Observation of non-Hermitian topology and its bulk–edge correspondence in an active mechanical metamaterial

Ananya Ghatak[a,1], Martin Brandenbourger[a,1], Jasper van Wezel[a,2], and Corentin Coulais[a,2]

[a]Institute of Physics, University of Amsterdam, 1098 XH, Amsterdam, The Netherlands

Edited by David A. Weitz, Harvard University, Cambridge, MA, and approved September 27, 2020 (received for review May 28, 2020)

Topological edge modes are excitations that are localized at the materials' edges and yet are characterized by a topological invariant defined in the bulk. Such bulk–edge correspondence has enabled the creation of robust electronic, electromagnetic, and mechanical transport properties across a wide range of systems, from cold atoms to metamaterials, active matter, and geophysical flows. Recently, the advent of non-Hermitian topological systems—wherein energy is not conserved—has sparked considerable theoretical advances. In particular, novel topological phases that can only exist in non-Hermitian systems have been introduced. However, whether such phases can be experimentally observed, and what their properties are, have remained open questions. Here, we identify and observe a form of bulk–edge correspondence for a particular non-Hermitian topological phase. We find that a change in the bulk non-Hermitian topological invariant leads to a change of topological edge-mode localization together with peculiar purely non-Hermitian properties. Using a quantum-to-classical analogy, we create a mechanical metamaterial with nonreciprocal interactions, in which we observe experimentally the predicted bulk–edge correspondence, demonstrating its robustness. Our results open avenues for the field of non-Hermitian topology and for manipulating waves in unprecedented fashions.

topological insulators | broken Hermiticity | mechanical metamaterials

The inclusion of non-Hermitian features in topological insulators has recently seen an explosion of activity. Exciting developments include tunable wave guides that are robust to disorder (1–3), structure-free systems (4, 5), and topological lasers and pumping (6–10). In these systems, active components are introduced to typically 1) break time-reversal symmetry to create topological insulators with unidirectional edge modes (1–5) and 2) pump topologically protected edge modes, thus harnessing Hermitian topology in non-Hermitian settings (6–9, 11). In parallel, extensive theoretical efforts have generalized the concept of a topological insulator to truly non-Hermitian phases that cannot be realized in Hermitian materials (12–14). However, such non-Hermitian topology and its bulk–edge correspondence remain a matter of intense debate. On the one hand, it has been argued that the usual bulk–edge correspondence breaks down in non-Hermitian settings, while on the other hand, new topological invariants specific to non-Hermitian systems have been proposed to capture particular properties of their edge modes (15–20).

Here, focusing on a non-Hermitian version of the Su–Schrieffer–Heeger (SSH) model (15–17, 21) with an odd number of sites (Fig. 1*A*), we find that a change in the bulk non-Hermitian topological invariant is accompanied by a localization change in the zero-energy edge modes. This finding suggests the existence of a bulk–edge correspondence for this type of truly non-Hermitian topology. We further construct a mechanical analogue of the non-Hermitian quantum model (Fig. 1*B*) and create a mechanical metamaterial (Fig. 1*C*) in which we observe the predicted correspondence between the non-Hermitian topological invariant and the topological edge mode. In particular, we report that the edge mode in the non-Hermitian topological phase has a peculiar nature, as it is localized on the rigid rather than the floppy side of the mechanical metamaterial.

Non-Hermitian Winding Number

The one-dimensional model depicted schematically in Fig. 1*A* is described by the quantum mechanical Bloch Hamiltonian

$$H(k)=\begin{pmatrix}0 & Q(k)\\ R(k) & 0\end{pmatrix}, \qquad [1]$$

where k is the wave vector. The coefficients $Q(k)=a_1+b_2\,e^{-ik}$ and $R(k)=a_2+b_1\,e^{ik}$ allow electrons to hop between neighboring sites within the unit cell (a_1 and a_2), as well as between unit cells (b_1 and b_2). If the amplitudes for hopping to the left (a_1 and b_1) are different from the corresponding amplitudes for hopping to the right (a_2 and b_2), the Hamiltonian is non-Hermitian, with complex eigenvalues $E_{\pm}(k)=\pm\sqrt{Q(k)R(k)}$ that come in pairs related by reflection in the point $E=0$. Thus Eq. **1** has a chiral symmetry, $\sigma_z^{-1}H(k)\sigma_z=-H(k)$, and falls in symmetry class AIII (12, 22).

A non-Hermitian Hamiltonian such as Eq. **1** may host two different types of topological invariants, corresponding either to a winding of the phase of their eigenvectors as the wave vector k is varied across the Brillouin zone (23) (Eq. **A1** in *Materials and Methods*) or to the complex energies winding around one another

Significance

In recent years, the mathematical concept of topology has been used to predict and harness the propagation of waves such as light or sound in materials. However, these advances have so far been realized in idealized scenarios, where waves do not attenuate. In this research, we demonstrate that topological properties of a mechanical system can predict the localization of waves in realistic settings where the energy can grow and/or decay. These findings may lead to strategies to manipulate waves in unprecedented fashions, for applications in vibration damping, energy harvesting, and sensing technologies.

Author contributions: J.v.W. and C.C. designed the research; A.G., J.v.W., and C.C. performed the theoretical calculations and the numerical simulations; M.B. and C.C. designed the experiments; A.G. and M.B. performed the experiments; A.G. and M.B. analyzed the data; and A.G., M.B., J.v.W., and C.C. wrote the paper.

The authors declare no competing interest.

This article is a PNAS Direct Submission.

[1]A.G. and M.B. contributed equally to this work.

[2]To whom correspondence may be addressed. Email: vanwezel@uva.nl or coulais@uva.nl.

This article contains supporting information online at https://www.pnas.org/lookup/suppl/doi:10.1073/pnas.2010580117/-/DCSupplemental.

First published November 9, 2020.

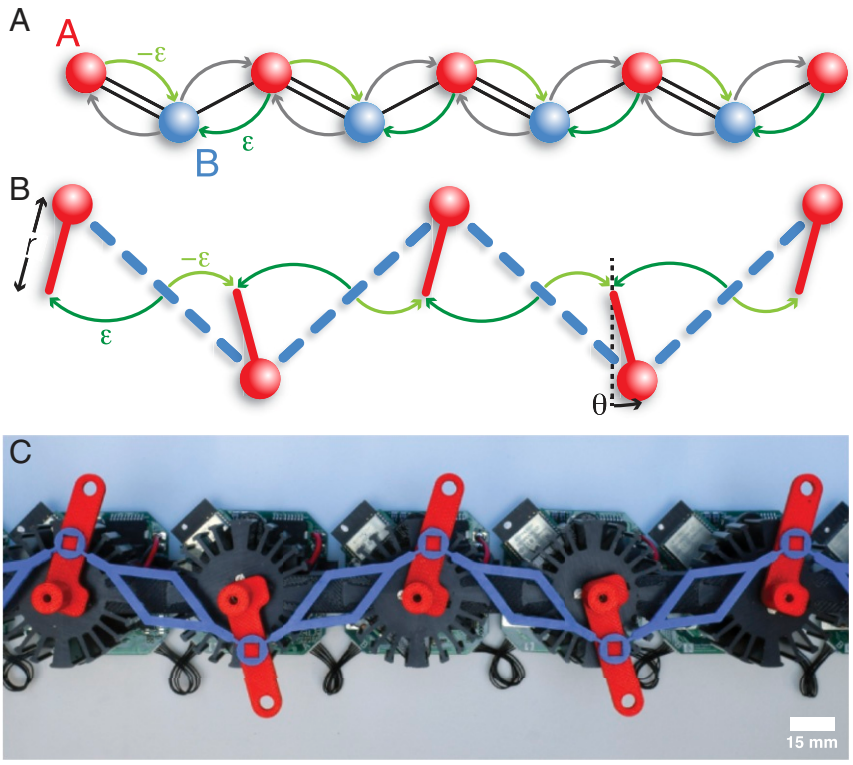

Fig. 1. Quantum-to-classical mapping of a chain with non-Hermitian topology. (*A*) An SSH chain with two sublattices, A (in red) and B (in blue), augmented with nonreciprocal variations in the hopping amplitudes (indicated by $\pm\varepsilon$). (*B*) The nonreciprocal classical analog of the augmented SSH chain, in which the classical masses (in red) correspond to the A sites in the quantum model, while the nonreciprocal springs (in blue) are analogous to the B sites. (*C*) Picture of the mechanical metamaterial realizing the nonreciprocal classical analogue of the augmented SSH model.

in the complex energy plane (12, 13) (Eq. **A2** in *Materials and Methods*). The former type of topology exists both for Hermitian and non-Hermitian systems, while the latter is exclusive to non-Hermitian systems, has not been observed yet, and is the focus of the present work.

Mapping between Non-Hermitian Quantum and Classical Models

The non-Hermitian topology contained in the model of Eq. **1** stems from the nonreciprocity of its hopping parameters. This renders a direct implementation within a quantum material challenging, but recent advances on nonreciprocal mechanical metamaterials (1–3, 24 suggest that such nonreciprocal interactions can be realized within a mechanical platform. In particular, inspired by the works of Kane and Lubensky (27) and Brandenbourger et al. (28), we introduce the one-dimensional mechanical system (Fig. 1*B*), which is described by the dynamical matrix:

$$D(k) = (-a + be^{-ik})(-a(1-\varepsilon) + b(1+\varepsilon)e^{ik}). \qquad [2]$$

Here, $a = (p + 2r\sin\theta)/\sqrt{p^2 + 4r^2\cos^2\theta}$ and $b = (p - 2r\sin\theta)/\sqrt{p^2 + 4r^2\cos^2\theta}$ are geometrical parameters that depend on the length r, the initial angle θ of the red rotors, and the lattice spacing p (Fig. 1*B* and *Materials and Methods*). The parameter ε modifies the stiffness of the blue springs in a nonreciprocal way, so that a strain in the spring causes a larger torque on the left rotor than on the right. This nonreciprocal interaction is created locally for each robotic unit cell by an active-control loop: the motor of each unit cell applies a torque that depends on the strain of its neighboring springs (*Materials and Methods*).

The equations of motion imposed by the dynamical matrix $D(k)$ on the displacements and their time derivatives may be combined into a Schrödinger-like equation, as proposed by Kane and Lubensky (27, 29–31). The matrix taking the place of the Hamiltonian in this formulation has precisely the same form as Eq. **1**, with $Q(k) = -a + be^{-ik}$ and $R(k) = -a(1-\varepsilon) + b(1+\varepsilon)e^{ik}$, but the eigenvalues represent frequencies $\omega_\pm(k)$, rather than the energies (*Materials and Methods*). This generalizes the formal mapping between the dynamical matrix $D(k)$ and the Hamiltonian $H(k)$ introduced by Kane and Lubensky (27) to a non-Hermitian setting.

Non-Hermitian Bulk–Edge Correspondence

In the following, we restrict our attention to a particular model with parameter values $a_1 = a$, $a_2 = a(1-\varepsilon)$, $b_1 = -b(1+\varepsilon)$, and $b_2 = -b$. In the reciprocal and non-Hermitian limit of $\varepsilon = 0$, the two bands of the model lie entirely on the real axis. As shown in Fig. 2, increasing ε leads to the bands developing imaginary components and eventually touching at the exceptional point $E = 0$ and $k = 0$ before coalescing. The non-Hermitian winding invariant ν then becomes one. At even larger values of ε, another exceptional point is encountered at $k = \pi$ and the bands separate again into a nonwinding phase.

We show the full phase diagram of this system in Fig. 3*A*, as a function of the hopping parameters a/b and the nonreciprocal parameter ε. In the hatched pink region, the complex energies (frequencies) wind, and the non-Hermitian topological invariant has the value $\nu = 1$. The other region has nonwinding non-Hermitian topology with $\nu = 0$, in accordance with the fact that the energies (frequencies) form disconnected bands. The phase boundaries correspond to the parameter values at which the bands coalesce at the exceptional point $E = 0$ (12–14)

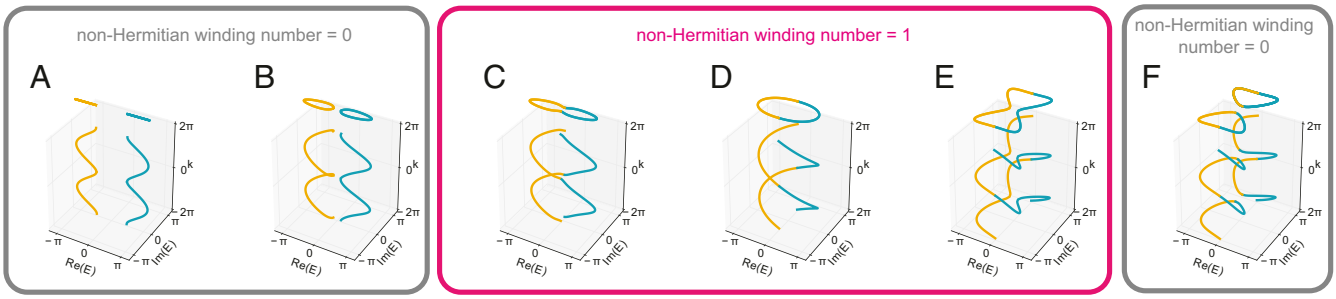

Fig. 2. Non-Hermitian topology. The real and imaginary parts of the energies (frequencies) of the two bands $E_-(k)$ [$\omega_-(k)$] (orange) and $E_+(k)$ [$\omega_+(k)$] (blue) as a function of wave number k, along with their projections onto the $k=0$ plane. The bands are shown for hopping parameters $a=2.5$ and $b=1$ and for six values of the nonreciprocal parameter ($\varepsilon=0$, 0.4, 0.45, 0.9, 2.3, and 2.4), grouped together into values corresponding from left to right to nonwinding (*A* and *B*), winding (*C*–*E*), and again nonwinding (*F*) non-Hermitian topology.

and are given by $\varepsilon_c=(a/b\pm1)/(a/b\mp1)$. The $\varepsilon=0$ axis represents the Hermitian limit, in which the non-Hermitian invariant is always zero and the two branches of exceptional points combine into a Dirac point at $a/b=1$. For the classical system, this axis corresponds precisely to the Kane–Lubensky model (27). The fact that the regions of non-Hermitian topology span large parts of parameter space suggests that they may be realized experimentally.

The hatched pink regions of the phase diagram Fig. 3*A* are based on the behavior of bulk topological invariants, calculated in a system with periodic boundary conditions. The non-Hermitian topology, however, is expected to be most visible experimentally in the emergence or suppression of edge modes localized at the edges of the chain. The edge modes can be found for the quantum (classical) model by solving Schrödinger's (Newton's) equation for zero-energy modes (*Materials and Methods*). We focus in the following on a SSH chain with an odd number of sites (Fig. 1*A*) and on the mechanical Kane–Lubensky chain (Fig. 1*B*), for which the bulk–edge correspondences are strictly equivalent. Namely, we investigate an SSH (Kane–Lubensky) chain with N A sites (rotors) and $N-1$ B sites (springs). There is a vast literature on even-sized SSH chains, and the choice of an odd-sized SSH chain can appear as less conventional. However, the topological nature of edge modes is the same for odd and even chains. Even in the Hermitian limit and for any given value of the topological invariant, it is the termination of the chain rather than the distinction between an odd and even number of atoms that determines the presence or absence of an edge mode. This can be clearly seen when considering, for example, the half-infinite chain, which is neither odd nor even and whose edge mode can be predicted to be present or absent based on knowledge of the invariant and the termination (32). Last but not least, choosing the odd chain is necessary to obtain a formal mapping with the mechanical system.

In the Hermitian limit $\varepsilon=0$, both the quantum and the classical chains always have a single zero mode, which is localized to the right (left) edge for $a>b$ ($a<b$) (green contours in Fig. 3*A*). In the non-Hermitian case $\varepsilon\neq0$, the zero mode changes sides precisely at the critical lines $\varepsilon=\varepsilon_c$ of the bulk, periodic system (Fig. 3*A*). In all cases, we find that the tails of the edge modes become oscillatory for $|\varepsilon|>1$ (Fig. 3 *B* and *C*), as a consequence of imaginary contributions to their eigenvectors. Other choices of parameters will lead to a qualitatively similar correspondence between edge-mode localization and bulk winding (*Materials and Methods*). Finally, we find that perturbations of the ideal model considered here, such as the inclusion of on-site potentials or mechanical bending interactions, progressively gap the system and suppress the zero modes (*Materials and Methods*).

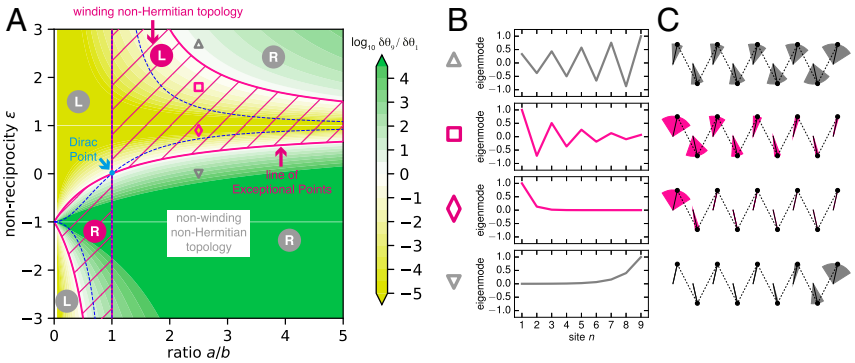

Fig. 3. Phase diagram and bulk–edge correspondence. (*A*) The phase diagram as a function of the parameters a/b and ε. The hatched pink region corresponds to the topological phase with winding complex energies and $\nu=1$, while the other regions are topologically nonwinding with two disconnected bands and $\nu=0$. The phase boundaries (thick solid pink lines) correspond to the bulk bands of the Bloch Hamiltonian touching the exceptional point $E=0$, at $\varepsilon=\varepsilon_c$. The thin dashed blue lines are defined by $\varepsilon=\varepsilon_s$ (*Materials and Methods*). The green contour plot represents the logarithm of the amplification factor of the zero edge mode for a chain of nine unit cells. The amplification factor is defined as $|\psi_9^A/\psi_1^A|$ ($|\delta\theta_9/\delta\theta_1|$) in the quantum (mechanical) system (*Materials and Methods*) and indicates the side at which the zero mode is localized. The inverted triangle, diamond, square, and triangle markers correspond to parameters $a/b=2.5$ and $\varepsilon=0$, 0.9, 1.8, and 2.7, respectively and indicate the parameters used for *B* and *C*. The (L) and (R) labels indicate whether the topological edge mode is localized on the left or the right, respectively. (*B*) Topological zero-energy modes of both the quantum model in Fig. 1*A* with nine (eight) A (B) sites—evaluated only at A sites, since the eigenmode at B sites is zero—and of the classical model in Fig. 1*B* with nine (eight) rotors (springs). (*C*) Graphical representation of the zero-energy modes for the mechanical chain. The opening angle of the colored wedges is proportional to the mode magnitude at each site.

The coincidence between the change of the non-Hermitian winding number and the change of localization of the zero modes demonstrates that these zero modes are topological and that a change of localization corresponds to a topological transition. These topological zero modes have several peculiar properties that are only possible because Hermiticity is broken: 1) increasing the nonreciprocity at a fixed value of the ratio a/b can be seen in Fig. 3*A* to cause two consecutive changes in the edge mode location, one of which goes against the direction of the nonreciprocal bias; 2) in the case of the quantum system, the shape of the phase diagram cannot be explained by a simple argument involving the shifting of unit cells, as can be done in the Hermitian limit; and 3) in the mechanical system, as the topological edge mode in the winding region occurs where the mechanical degrees of freedom are constrained—this is a zero-energy mode, and yet it involves stretching of the springs.

The bulk–edge correspondence shown in Fig. 3*A* differs from but is complementary to recent results on even non-Hermitian SSH chains, where the topological modes appear or disappear at the values $\varepsilon_s = ((a/b)^2 \pm 1)/((a/b)^2 \mp 1)$ at which the gap of the open chain is closed (15, 16). That the gap closings of the open and closed chain do not coincide is a manifestation of the non-Hermitian skin effect, which also causes all modes in the system except the topological zero mode to localize on one end of the chain (*Materials and Methods*) (15, 17, 18, 21, 28, 33). Recent results show that taking into account the non-Hermitian skin effect allows the definition of a non-Bloch topological invariant, which switches value at ε_s (15, 16). A physically compelling picture thus emerges for non-Hermitian topological phases: while the winding topological invariant predicts the edge at which the topological zero modes are localized, the non-Bloch invariant predicts the existence of the topological modes and the location of the gap closing.

Non-Hermitian Bulk–Edge Correspondence in an Active Mechanical Metamaterial

To demonstrate the non-Hermitian bulk–edge correspondence described in *Non-Hermitian Bulk–Edge Correspondence*, we provide an experimental realization. To this end, we build an active mechanical metamaterial (Figs. 1*C* and 4*A*), which consists of nine robotic unit cells and in which a combination of geometry and active control is used to implement $D(k)$, as defined in Eq. **2**. While the geometry allows us to obtain suitable values of $a = 1.00$ and $b = 0.73$, active control makes it possible to tune the nonreciprocal parameter ε (*Materials and Methods*). We selectively access properties of the periodic (bulk) or open (edged) system by either including or omitting a rigid connection between the first and last unit cells (Fig. 4*A* and *Materials and Methods*).

In this setup, we first perform relaxation experiments on the periodic metamaterial to quantify directly the bulk eigenfrequencies for the wave vectors $k = 0, \pi$ and hence the bulk topological invariant ν (Fig. 4 *A*–*D*). We find that the non-Hermitian topological invariant jumps from zero—where the eigenfrequencies are disconnected as in Fig. 4*B*—to one—where the eigenfrequencies wind as in Fig. 4*C*—for a nonreciprocal parameter $\varepsilon_c^{\text{periodic}} = 0.12$ (Fig. 4*D*). Second, we probe the signature of the zero modes of the open chain (Fig. 4*E*) by applying a low-frequency excitation at the central unit cell. We observe a right-to-left (left-to-right) decaying displacement field for small (large) values of the nonreciprocal parameter ε (Fig. 4*F* and Movie S1). We find that the amplification factor $|\delta\theta_9/\delta\theta_1|$ crosses the value 1 at a critical value of $\varepsilon_c^{\text{open}} = 0.12$ (Fig. 4*G*). Remarkably, the correspondence $\varepsilon_c^{\text{periodic}} = \varepsilon_c^{\text{open}}$ agrees precisely with the theoretically predicted non-Hermitian bulk–edge correspondence. It shows that the experimentally observable switching of edge-state localization in the open chain coincides with the changing value of the non-Hermitian topological invariant in the (bulk) system with periodic boundary conditions. Moreover, it proves the robustness of both the bulk–boundary correspondence and the non-Hermitian topology to inherent deviations from the ideal model such as geometric and motor nonlinearities, spring bending, time delays and noise in the microcontrollers, friction, and geometric irregularities.

To show more clearly the connection between the topological transition and the behavior of the edge modes, we also create a domain wall in the metamaterial, with the leftmost part remaining reciprocal ($\varepsilon = 0$) and the nonreciprocal parameter ε being tuned away from zero in the rightmost part (Fig. 5*C*) and vice versa (Fig. 5*D*). As expected, beyond the threshold value, the localization of the displacement field changes from the right edge to the domain boundary at the center (Fig. 5*C*) or the displacement field localizes at both edges away from the domain boundary (Fig. 5*D*).

Discussion and Outlook

To conclude, we discovered and experimentally observed a type of bulk–edge correspondence for the non-Hermitian topological phase of a mechanical metamaterial with nonreciprocal interactions. This particular form of non-Hermitian bulk–edge correspondence, connected to energy winding, exhibits marked differences with the recently proposed non-Hermitian bulk–edge correspondence connected to a biorthogonal expectation value (15, 16). First, the correspondence based on energy winding reported here is unaffected by the non-Hermitian skin effect: despite the complete reorganization of the spectrum between a periodic and an open system, the energy winding of the periodic system predicts changes in the edge modes of the open system. Second, the energy winding and the biorthogonal condition both predict the emergence of zero modes. However, while the biorthogonal condition predicts the existence of edge modes, the energy winding additionally predicts the side of the chain at which the topological mode appears. These differences call for further investigation and generalization of the bulk–edge correspondence based on energy winding, beyond the particular system considered here.

Further, we envision the study of nonlinearity, robustness to disorder, different interactions, higher spatial dimensions, and other strategies to achieve non-Hermiticity to be exciting future research directions. We believe that our work provides conceptual and technological advances, opening up avenues for the topological design of tunable wave phenomena.

Materials and Methods

Hermitian and Non-Hermitian Topology of the Nonreciprocal SSH Model. The Hamiltonian of Eq. **1** may acquire topological character either from the winding of the Berry connection determined by its eigenfunctions $|\psi^{\pm}(k)\rangle$ or from the direct winding of its eigenenergies $E^{\pm}(k)$ in the complex plane. While the former type of winding corresponds to conventional Hermitian topology (29), the latter corresponds to a unique form of non-Hermitian topology that can only exist when the eigenenergies are complex (12, 13). The Hamiltonian in Eq. **1** is pseudo-Hermitian with respect to a positive definite metric operator (34) and can be diagonalized to find its eigenenergies $E^{\pm}(k) = \pm\sqrt{R(k)Q(k)}$ as well as its left and right eigenmodes, $\langle\psi_L^+(k)| = \left(1, \sqrt{\frac{Q(k)}{R(k)}}\right)$, $\langle\psi_L^-(k)| = \left(-\sqrt{\frac{R(k)}{Q(k)}}, 1\right)$, $|\psi_R^+(k)\rangle = \left(1, \sqrt{\frac{R(k)}{Q(k)}}\right)^T$, and $|\psi_R^-(k)\rangle = \left(-\sqrt{\frac{Q(k)}{R(k)}}, 1\right)^T$. These eigenmodes obey the biorthonormality condition, and the Hamiltonian preserves a generalized unitarity condition (34). To compute the conventional Hermitian topological invariant in the non-Hermitian setting, we can define the Berry connection (14) as $\mathcal{A}^{\pm}(k) = -i\langle\psi_L^{\pm}(k) \mid \partial_k\psi_R^{\pm}(k)\rangle$, from which the topological invariant is then calculated to be

$$\gamma^{\pm} = \frac{1}{2\pi}\int_0^{2\pi} dk A^{\pm}(k). \qquad \textbf{[A1]}$$

Choosing different left and right eigenvectors in the definition of the Berry connection, or introducing a modified inner product, does not yield additional invariants (14). The invariants $\gamma^{\pm}$ are zero (when $a/b > 1$) or integer

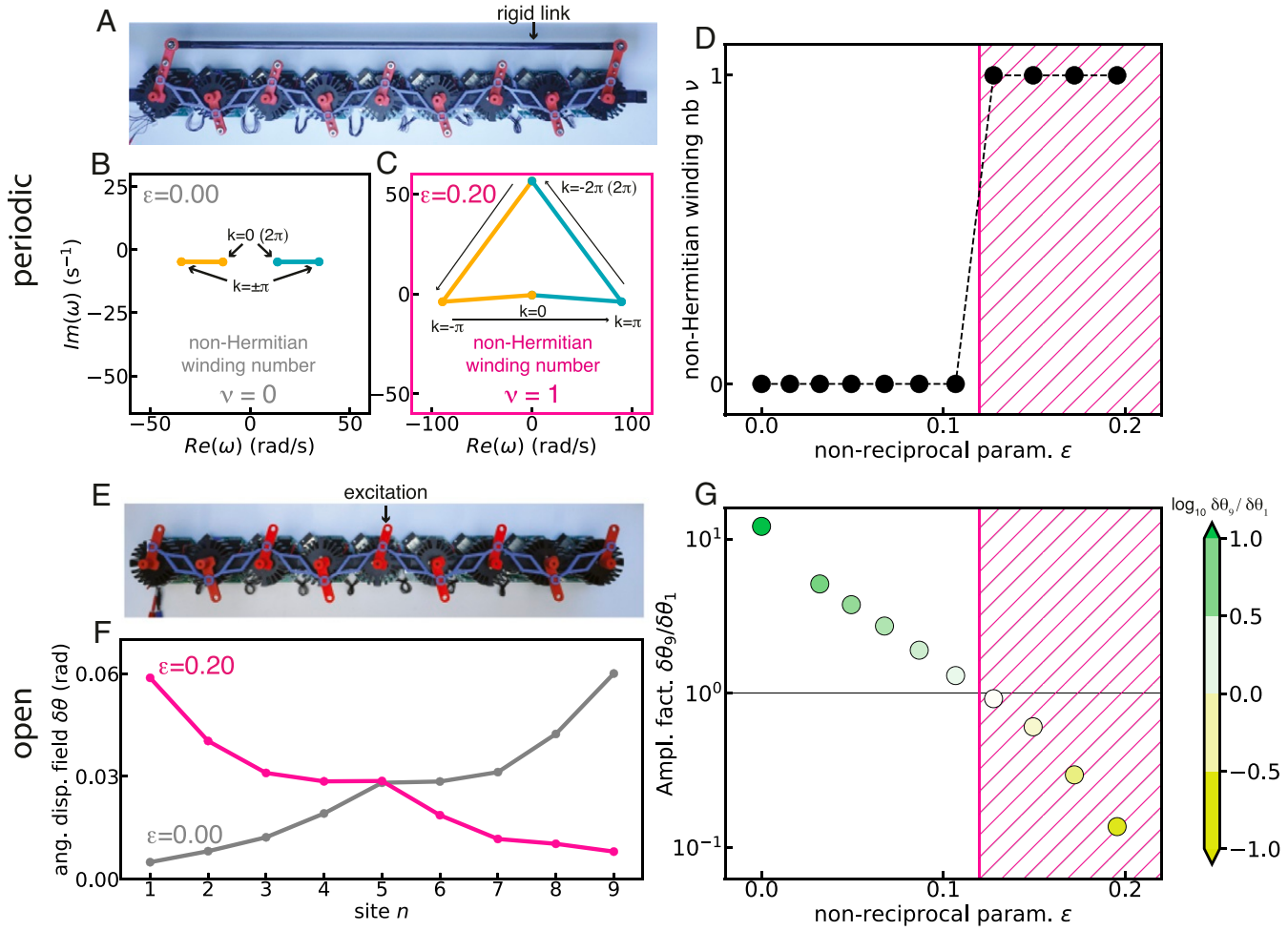

Fig. 4. Experimental observation of the non-Hermitian bulk–edge correspondence. (*A*) Picture of the periodic metamaterial with nine unit cells, wherein the first and last rotors are rigidly connected. (*B* and *C*) Band diagrams showing the real part vs. the imaginary part of the eigenfrequencies for a nonreciprocal parameter $\varepsilon = 0.00$ (*B*) and $\varepsilon = 0.20$ (*C*). In *B*, the two bands are disconnected (nonwinding non-Hermitian topology), while in *C*, they are connected (winding). (*D*) Corresponding measurement of the non-Hermitian winding number ν vs. nonreciprocal parameter ε. (*E*) Picture of the open metamaterial with nine unit cells. (*F*) Angular displacement field for different values of the nonreciprocal parameter ε, upon low-frequency excitation of the central unit for $\varepsilon = 0.00$ (gray) and $\varepsilon = 0.20$ (pink). (*G*) Amplification factor $\delta\theta_9/\delta\theta_1$ vs. nonreciprocal parameter ε. The hatched pink regions in *D* and *G* depict the non-Hermitian winding phase for $\varepsilon > \varepsilon_c^{\text{periodic}}$ and $\varepsilon > \varepsilon_c^{\text{open}}$, respectively. The marker color map quantifies the amplification factor, as in Fig. 3*A*. Details of the measurement protocols are in *Materials and Methods*. See also Movie S1.

(when $a/b < 1$) for the regions with nonwinding non-Hermitian topology (nonhatched regions in Fig. 3*A*). In the winding non-Hermitian topological regions (pink hatched regions in Fig. 3*A*), the two bands coalesce into a 4π-periodic structure. In that case, the Berry connection winds an integer number of times after integration over the full 4π period, and we find $\frac{1}{2\pi}\int_0^{4\pi} dk A^{\pm}(k) = 1$ for the single, coalesced band. The truly non-Hermitian topology can be defined in terms of the winding of eigenenergies around an exceptional point, as shown in Fig. 2. The corresponding winding number can be calculated to be

$$\nu = -\frac{1}{2\pi}\int_0^{4\pi} dk \frac{\partial}{\partial k}(\arg[E^+(k) - E^-(k)]). \qquad \textbf{[A2]}$$

The value of this non-Hermitian topological invariant is shown in Fig. 3*A*. Notice that the definition of Eq. **A2** differs by a factor of two from the convention used in some other works (13).

Edge Modes of the Nonreciprocal SSH Model with an Odd Number of Sites. In Eq. **1**, a nonreciprocal version of the SSH model is defined in reciprocal space. Here, we use the corresponding real space formulation to identify the edge modes of a finite nonreciprocal SSH chain with open-boundary conditions. Specifically, we consider N sites of type A and $N-1$ sites of type B, which is strictly analogous to the mechanical Kane–Lubensky chain (27). The Hamiltonian is given in real space by

$$\mathbf{H} = \begin{pmatrix} 0 & a_1 & 0 & & \cdots & & 0 \\ a_2 & 0 & b_1 & & & & \\ 0 & b_2 & 0 & a_1 & \ddots & & \vdots \\ & & a_2 & 0 & \ddots & & \\ \vdots & & \ddots & \ddots & \ddots & a_1 & 0 \\ & & & & a_2 & 0 & b_1 \\ 0 & & \cdots & & 0 & b_2 & 0 \end{pmatrix}, \qquad \textbf{[A3]}$$

where a_1, a_2, b_1, and b_2 are hopping coefficients, which we assume to be real. In the Hermitian case, with $a_1 = a_2$ and $b_1 = b_2$, the Hamiltonian has a unique zero mode satisfying the equation $\mathbf{H}|\psi\rangle = \mathbf{0}$, with the eigenmode written as $|\psi\rangle = (\psi_1^A, \psi_1^B, \ldots, \psi_{N-1}^A, \psi_{N-1}^B, \psi_N^A)^T$. However, in the generic non-Hermitian case considered here, with $a_1 \neq a_2$ and $b_1 \neq b_2$, the equations $\mathbf{H}|\psi_R\rangle = \mathbf{0}$ and $\langle\psi_L|\mathbf{H} = \mathbf{0}$, respectively, for the right and left eigenvectors may yield distinct zero-energy modes. We solve these two equations and find $(\psi_n^A)_R/(\psi_1^A)_R = (-a_2/b_1)^{n-1}$, $(\psi_n^B)_R = 0$ for the right eigenmode, and $(\psi_n^A)_L/(\psi_1^A)_L = (-a_1/b_2)^{n-1}$, $(\psi_n^B)_L = 0$ for the left eigenmode. In Fig. 3*B*, we only plot the right eigenmodes for $a_1 = a$, $a_2 = a(1-\varepsilon)$, $b_1 = -b(1+\varepsilon)$, and $b_2 = -b$.

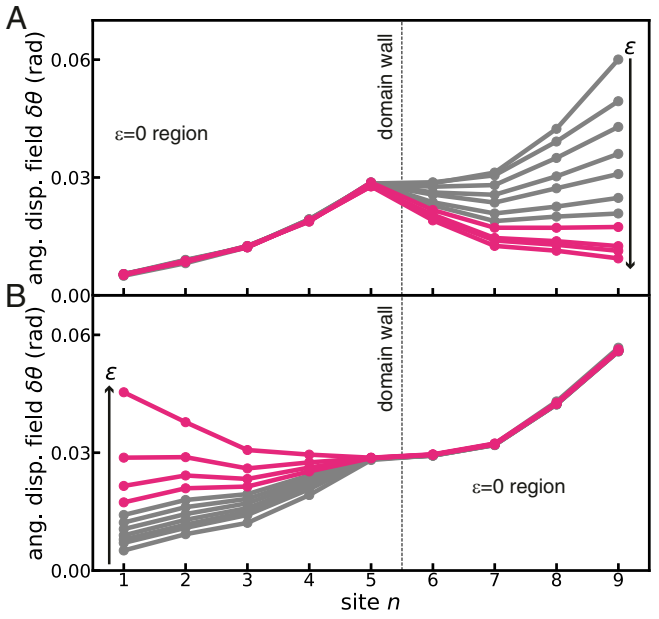

Fig. 5. Domain wall. (*A* and *B*) Experimentally measured angular displacement field for different values of the nonreciprocal parameter ε, upon low-frequency excitation of the central unit. Data for $\varepsilon < 0.12$ ($\varepsilon > 0.12$) are shown in gray (pink). The metamaterial has a domain wall. The rightmost (*A*) or leftmost (*B*) part of the metamaterial is set to $\varepsilon = 0$, while the leftmost (*A*) or rightmost (*B*) part of the metamaterial has the values of the nonreciprocal parameter $\varepsilon = [0.00, 0.02, 0.03, 0.05, 0.07, 0.09, 0.11, 0.13, 0.15, 0.17, 0.20]$.

Non-Hermitian Skin Effect. In the non-Hermitian case, boundary conditions have a significant effect on the shape of the entire spectrum, namely open boundaries shift modes at all energies (frequencies) toward one side of the chain, in what is known as the non-Hermitian skin effect (15, 17, 33, 35). This effect is not related to topology and was recently observed in both a nonreciprocal mechanical metamaterial (28) and a nonreciprocal electronic circuit (18). Theoretically, it has been shown that in a non-Hermitian SSH chain, the closing of the bandgap appears at parameter values that are different for open and periodic boundary conditions, in an apparent breakdown of the bulk–edge correspondence (15–17, 35) (indicated by the gray region in Fig. 6*B*). We find consistent results (indicated by the gray region in Fig. 6*A*), but we report in addition a clear correspondence between the topology of the bulk spectrum computed with closed-boundary conditions and the zero-energy edge modes obtained with open-boundary conditions: 1) a zero-energy edge mode always exists, as calculated analytically in the section above and confirmed numerically (Fig. 6*A*); 2) this edge mode in the chain with open boundaries changes its localization at the exceptional points of the periodic—bulk— model (Fig. 3 *A* and *B*); and 3) surprisingly, this edge mode is unaffected by the gap closing $\varepsilon = (a^2/b^2 \pm 1)/(a^2/b^2 \mp 1)$ of the open chain (15) (dashed lines in Fig. 3*A* and Fig. 6). These results are consistent with and complementary to recent results in the case of the even non-Hermitian SSH chain (15, 16).

Notice that in our system, a signature of the non-Hermitian skin effect can be seen in the response to a local excitation. While the localization of the response at low frequency (Fig. 7*A*) is essentially the same as that of the zero mode (Fig. 3), changing localization edge at the topological phase boundaries, the localization at large frequencies (Fig. 7*B*) solely depends on the nonreciprocal parameter, which is a direct signature of the non-Hermitian skin effect. For extensive portions of parameter space, the localization of the topological zero mode dominating the low-frequency response is opposite to that induced by the non-Hermitian skin effect at high frequencies.

Nonreciprocal Kane–Lubensky Chain. The classical analog of the non-Hermitian SSH chain is a nonreciprocal version of the Kane–Lubensky chain (27), as shown in Fig. 1*B*. In this system, N rotors of length r, with an initial tilt angle θ and a staggered orientation, are connected by $N-1$ springs between subsequent rotors, with lattice spacing p. To construct the equation of motion for such a system, we first write the relation between the angular displacements of the rotors, $|\delta\theta\rangle = (\delta\theta_1, \ldots, \delta\theta_N)^T$, and the length change of the springs (positive for stretching, negative for compression), $|\delta\ell\rangle = (\delta\ell_1, \ldots, \delta\ell_{N-1})^T$. This is given by $|\delta\ell\rangle = \mathbf{R}\,|\delta\theta\rangle$, with the compatibility matrix (29):

$$\mathbf{R} = r\cos\theta \begin{pmatrix} -a & b & 0 & \ldots & 0 \\ 0 & -a & b & & \vdots \\ \vdots & & \ddots & \ddots & 0 \\ 0 & \ldots & 0 & -a & b \end{pmatrix}. \qquad \text{[A4]}$$

The coefficients $a = (p - 2r\sin\theta)/\sqrt{p^2 + 4r^2\cos^2\theta}$ and $b = (p + 2r\sin\theta)/\sqrt{p^2 + 4r^2\cos^2\theta}$ are geometric parameters (27). We can similarly write the relation between the torque on each rotor, $|\tau\rangle = (\tau_1, \ldots, \tau_N)^T$, and the tension in the springs, $|t\rangle = (t_1, \ldots, t_{N-1})^T$, in the form $|\tau\rangle = \mathbf{Q}\,|t\rangle$, where $\mathbf{Q}$ is the equilibrium matrix. In the Hermitian case, $\mathbf{R}$ and $\mathbf{Q}$ are transposes of each other (29). The compatibility and equilibrium matrices can be multiplied to compute the so-called dynamical matrix $\boldsymbol{D}^{\text{Hermitian}} = \frac{k}{J}\boldsymbol{QR}$, where k is the spring constant of the elastic link between subsequent rotors, and J is the rotational moment of inertia of the rotors. In the active mechanical metamaterial, each unit cell n has a local control system that can apply a local torque $\tau_n^{\text{controlloop}}$ that depends on the angular displacement of its rotor $\delta\theta_n$ and that of its neighbors $\delta\theta_{n-1}$ and $\delta\theta_{n+1}$. We choose to apply the following torque: $\tau_n^{\text{controlloop}} = \varepsilon k r^2\cos^2\theta(b(b\delta\theta_n - a\delta\theta_{n-1}) - a(a\delta\theta_n - b\delta\theta_{n+1}))$. Since the added torques are proportional to the angular displacements, the system can still be described by an effective dynamical matrix $\boldsymbol{D} = \boldsymbol{D}^{\text{Hermitian}} + \boldsymbol{D}^{\text{controlloop}}$ of the form

$$\mathbf{D} = \frac{kr^2\cos^2\theta}{J} \times \begin{pmatrix} a^2(1-\varepsilon) & -ab(1+\varepsilon) & 0 & & \\ -ab(1-\varepsilon) & a^2(1-\varepsilon)+b^2(1+\varepsilon) & -ab(1+\varepsilon) & & \\ 0 & -ab(1-\varepsilon) & a^2(1-\varepsilon)+b^2(1+\varepsilon) & & \\ & & & \ddots & \\ 0 & & 0 & & - \end{pmatrix} \begin{pmatrix} 0 & - & - & 0 \\ 0 & - & - & 0 \\ -ab(1+\varepsilon) & - & - & 0 \\ \ddots & \ddots & & \\ - & 0 & -ab(1-\varepsilon) & b^2(1+\varepsilon) \end{pmatrix}, \qquad \text{[A5]}$$

which is nonsymmetric for $\varepsilon \neq 0$. In Eq. **2**, we assume that the ratio $kr^2\cos^2\theta/J = 1$ without loss of generality. We compute the right and left zero modes by solving $\mathbf{D}\,|\delta\theta_R\rangle = \mathbf{0}$ and $\langle\delta\theta_L|\,\mathbf{D} = \mathbf{0}$, and we find $(\delta\theta_n)_R/(\delta\theta_1)_R = (a(1-\varepsilon)/b(1+\varepsilon))^{n-1}$ and $(\delta\theta_n)_L/(\delta\theta_1)_L = (a/b)^{n-1}$, respectively. In the rest of the paper, we show and discuss only the right zero modes, because the right zero modes dominate the observed angular displacement profile (36). With periodic boundary conditions, the Fourier transform of Eq. **A5** becomes $D(k) = a^2(1-\varepsilon) + b^2(1+\varepsilon) - ab(1+\varepsilon)e^{ik} - ab(1-\varepsilon)e^{-ik}$, which in its factored form $D(k) = Q(k)R(k)$, with $Q(k) = (-a + be^{-ik})$, $R(k) = (-a(1-\varepsilon) + b(1+\varepsilon)e^{ik})$ coincides with Eq. **2**. This factored mathematical expression allows us to construct the mapping between quantum and classical systems, following refs. 27 and 29–31, where the quantum Hamiltonian is written as in Eq. **1**. Notice that the physical meaning of the Fourier equilibrium and compatibility matrices $Q(k)$ and $R(k)$ is ill-defined in the non-Hermitian case.

Role of Perturbations. The computational model introduced in Eq. **A5** and discussed in *Non-Hermitian Bulk–Edge Correspondence* is necessarily an idealization. In the actual mechanical, integrated system in the experimental setup, there are unavoidable small effects of bending in each of the elastomeric bands, on top of other essential effects from frictional forces, geometrical and electromechanical nonlinearities in the chain, time delays and noise from microcontrollers, and geometric irregularities. That we nevertheless see the theoretically predicted bulk–edge correspondence in our experimental results is thus witness to the robustness of the non-Hermitian topology described by the numerical predictions. To test the limits of the topological robustness, we explicitly probe the role of two types of perturbations in the numerical model: 1) bending interactions inherently present in the elastomeric bands connecting the nearest-neighbor rotors and 2) an on-site potential. With these, the Fourier-transformed dynamical matrix becomes $D(k) = a^2(1-\varepsilon+\rho+g) + b^2(1+\varepsilon+\rho+g) - ab(1+\varepsilon-\rho)e^{ik} - ab(1-\varepsilon-\rho)e^{-ik}$, where ρ is the relative bending stiffness of

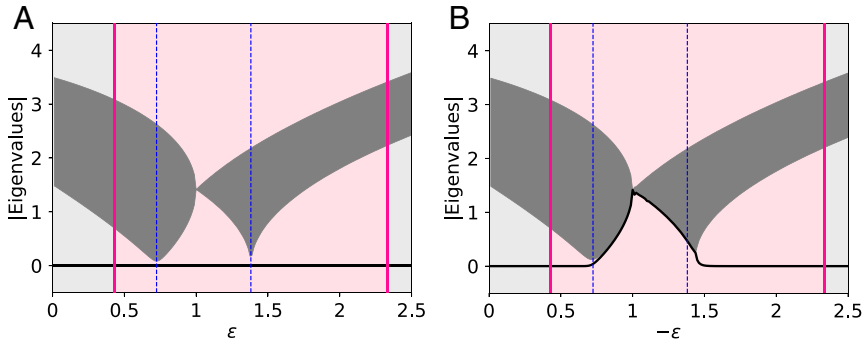

Fig. 6. Spectra with open-boundary conditions. (*A*) Eigenvalues of an odd finite non-Hermitian SSH chain with 50 A sites and 49 B sites with open-boundary conditions, plotted as a function of the nonreciprocal parameter ε. Here, we used parameters values $a = 2.5$ and $b = 1$, as in Figs. 2 and 3. The black line corresponds to the lowest energy mode and the gray band to the region enclosing the rest of the spectrum. The pink region is delimited by thick solid pink lines and indicates the values of ε for which the bulk energies (computed with periodic boundary conditions) wind. The zero-energy mode of the open chain changes its localization as ε is tuned into or out of this region. The dashed blue lines show the values of ε for which the spectrum of the open chain become gapless and correspond to a jump of the non-Bloch invariant defined in ref. 15. (*B*) Eigenvalues of an even finite non-Hermitian SSH chain with 50 A sites and 50 B sites. Here, we used $a = 1$ and $b = 2.5$ to ensure that an edge state exists when the nonreciprocal parameter ε crosses the critical values indicated by thick pink lines. The indicated regions and lines have the same meaning as in *A*, but in this case, the lowest energy mode is always doubly degenerate, with one mode changing localization at the thick pink lines. That the gap closing in the open chain does not seem to coincide with the blue dashed line is due to the finite size of the chain used.

each rubber band, and g is the on-site potential. For the system with periodic boundary conditions, described by $D(k)$, the phase boundaries between nonwinding non-Hermitian topology and winding non-Hermitian topology become

$$\varepsilon_c = \frac{a/b \pm 1}{a/b \mp 1} + \rho \frac{a/b \mp 1}{a/b \pm 1} + g \frac{(a/b)^2 + 1}{(a/b)^2 - 1}. \qquad \textbf{[A6]}$$

Fig. 8 *A* and *B* shows that the presence of bending gaps the spectrum of the model with periodic boundary conditions around $\varepsilon = 0$ for all values of the ratio a/b. At higher values of nonreciprocal parameter ε, however, the transition into a phase with non-Hermitian topology survives. Likewise, for nonzero on-site potential, the gapping of the spectrum in the periodic chain causes a breakdown of the bulk–boundary correspondence around the point $a/b = 1$ and $\varepsilon = 0$, while for higher values of ε, it survives (Fig. 8 *C* and *D*). Both of these observations are a testament to the robustness of the non-Hermitian topology and its bulk–boundary correspondence, which remain intact even in the presence of perturbations, for sufficiently large values of the nonreciprocity. These considerations have been taken into account in the design of the experiments described in *Experimental Platform*, wherein a specific shape of the rubber band is chosen to minimize the bending.

Experimental Platform. To perform the experiments, we followed Brandenbourger et al. (28) and created a one-dimensional, nonreciprocal active mechanical metamaterial (Fig. 1*C*) consisting of nine unit cells, each of which has a single rotational degree of freedom θ_n, where n is the unit cell index. The unit cells are mechanically connected in a specific geometry initially proposed by Kane and Lubensky (27) (Fig. 1*B*). Each unit cell consists of a rigid rotor of 36 mm in length and initial angle $(-1)^n(\theta - \pi/2)$ with respect to the horizontal axis, where $\theta = \pi/12$. Each rotor is connected to its neighbors at its midpoint, $r = 18$ mm, by a flexible, laser-cut elastomeric band of 4-mm thickness, whose shape has been optimized such that the band can easily hinge at its anchoring points and such that in-plane compression and stretching of the band dominates its elastic response (Fig. 1*C*). The lattice spacing between subsequent rotors is $p = 60$ mm. Assuming that the bending of the band and friction can be neglected, to linear order, the deformations of the elastomeric bands induce a torque on rotor n given by $\tau_n^{\text{elastic}} = kr^2 \cos^2\theta(a(a\delta\theta_n - b\delta\theta_{n+1}) - b(b\delta\theta_n - a\delta\theta_{n-1}))$, where $\delta\theta_n$ is the angular displacement with respect to the initial angle in the reference state, $k = 7.8 \times 10^{-3}$ N/m is the spring constant of the rubber band, and $a = 1.00$ and $b = 0.73$ are the geometric parameters defined above. In addition, each robotic unit cell is made of a mechanical oscillator, an angular encoder (Broadcom HEDR-55L2-BY09), a direct-current coreless motor (Motraxx CL1628), a microcontroller (Espressif ESP 32), and a custom-made electronic board that connects these components and ensures power conversion and communication between neighboring unit cells. Each robotic unit cell uses a local active control loop to apply a strain-dependent torque on rotor n given by $\tau_n^{\text{controlloop}} = \varepsilon kr^2 \cos^2\theta(b(b\delta\theta_n - a\delta\theta_{n-1}) - a(a\delta\theta_n - b\delta\theta_{n+1}))$, where ε is a tunable dimensionless nonreciprocal gain parameter. The total torque on the rotors then realizes effective nonreciprocal interactions,

$$\tau_n = kr^2 \cos^2\theta \left(-ab(1-\varepsilon)\delta\theta_{n-1} + (a^2(1-\varepsilon) + b^2(1+\varepsilon))\delta\theta_n - ab(1+\varepsilon)\delta\theta_{n+1}\right), \qquad \textbf{[A7]}$$

where $\tau_n = \tau_n^{\text{elastic}} + \tau_n^{\text{controlloop}}$. This system precisely realizes the dynamical matrix $\boldsymbol{D}$ defined in Eq. **A5**, and therefore its mechanical response exhibits

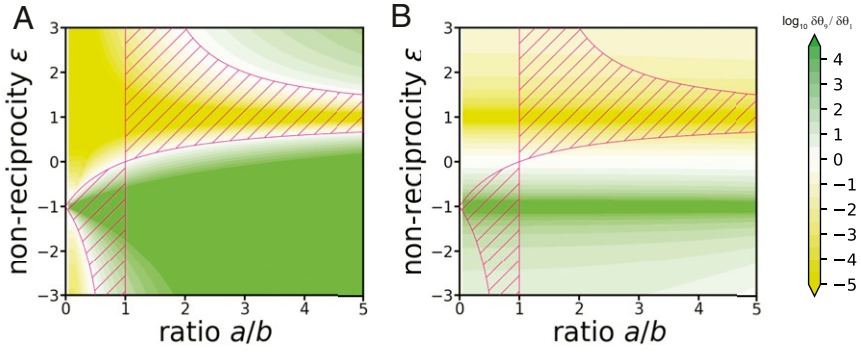

Fig. 7. Signature of the non-Hermitian skin effect. Amplification factor for an excitation at a dimensionless radial frequency $\omega = 0.01$ (*A*) and $\omega = 10$ (*B*) for the metamaterial. The hatched pink region depicts the non-Hermitian topological phase. Notice that the localization of the low-frequency topological response is opposite to that of the high-frequency skin effect in extensive regions of parameter space.

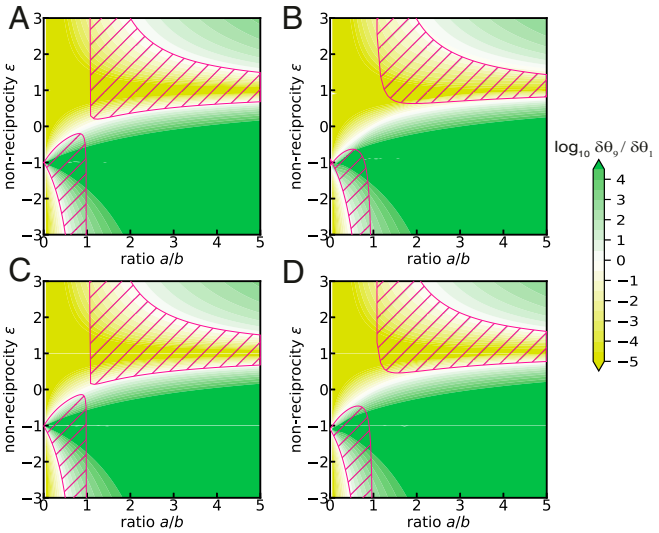

Fig. 8. Role of perturbations. The evolution of the phase diagram as a function of bending (*A* and *B*) and on-site potential (*C* and *D*). The phase diagram is shown for two different values of the bending stiffness parameter $\rho = 0.01$ (*A*) and $\rho = 0.1$ (*B*) and two different values of the on-site potential $g = 0.01$ (*C*) and $g = 0.1$ (*D*). The hatched pink region indicates the phase with winding non-Hermitian topology given by Eq. **A6**, in which the model with periodic boundary conditions has winding eigenvalues. The color scale shows the amplification factor in the model with open-boundary conditions.

the bulk–edge correspondence shown by the right zero modes of ***D***. We record the rotors' instantaneous positions $\delta\theta_n(t)$ via the angular encoders at a resolution of 4.4×10^{-4} rad and a sampling frequency 100 Hz.

Measurements of the Non-Hermitian Winding Number. In order to measure the winding of the bands in the spectrum of the system with periodic boundary conditions, we connect the first and the last rotors with a rigid bar and ball-bearing hinges. To ensure homogeneity of the moments of inertia throughout the system, we add small masses at the end of each rotor. A rigid pin is attached to each rotor. We impose the initial position of each rotor $\delta\theta_n(t=0)$ away from their equilibrium position as follows: for each wave vector k, we manufacture drilled rigid plates with precisely positioned holes, in which the rigid pins can be inserted and that set the initial condition. The initial condition $\delta\theta_n(t=0) = \bar{\delta\theta}\cos kn$ is chosen such that the overall configuration of the chain is modified from equilibrium according to a specific wave vector ($k = 0$ or $k = \pi$). In order to stay in the linear regime as well as within the limit of angular resolution, we impose $\bar{\delta\theta} = 0.21$ and 0.04 rad, respectively, for the measurements on the wave vectors $k = 0$ and $k = \pi$. We remove rapidly the drilled plate to let the system freely relax. For each experiment, every unit cell is observed to relax the same way, except for their phase. For each wave vector k, we fit the displacement overtime of the far left unit cell to the equation $(A_1 \exp(\lambda_k t) + A_2 \exp(\lambda'_k t))\cos(\omega_k t)$ to deduce the real (imaginary) parts of the eigenfrequencies ω_k (λ_k and λ'_k) (Fig. 4 *B* and *C*). From there, we use a discretized version of Eq. **A2**

$$\nu = -\frac{2}{\pi}\left(\arctan\frac{\lambda_\pi - \lambda'_\pi}{2\omega_\pi} - \arctan\frac{\lambda_0 - \lambda'_0}{2\omega_0}\right) \qquad \textbf{[A8]}$$

to compute the winding invariant as a function of ε, as shown in Fig. 4*D*.

Measurements of the Edges Modes. We excite the metamaterial at the center rotor ($n = 5$) by applying sinusoidal oscillations of amplitude 0.028 rad and frequency 0.05 Hz over five periods of oscillations. We extract the magnitude of the oscillation of each rotor via a Fourier series analysis to produce the data shown in Fig. 4 *F*–*E*.

Data Availability. Automation codes and raw and postprocessed data for the experiments have been deposited in Github (https://github.com/corentincoulais/nHtopo_1DactiveMM.git).

ACKNOWLEDGMENTS. We thank D. Giesen, T. Walstra, and T. Weijers for their skillful technical assistance. We are grateful to C. Bender, L. Fu, T. Lubensky, D. Z. Rocklin, R. Thomale, and Z. Wang for insightful discussions and to M.S. Golden for critical review of the manuscript. J.v.W. acknowledges funding from a Netherlands Organization for Scientific Research Vidi grant. C.C. acknowledges funding from European Research Council Grant ERC-StG-Coulais-852587-Extr3Me.

1. L. M. Nash *et al.*, Topological mechanics of gyroscopic metamaterials. *Proc. Natl. Acad. Sci. U.S.A.* **112**, 14495–14500 (2015).
2. N. P. Mitchell, L. M. Nash, D. Hexner, A. M. Turner, W. T. M. Irvine, Amorphous topological insulators constructed from random point sets. *Nat. Phys.* **14**, 380–385 (2018).
3. A. B. Khanikaev, R. Fleury, S. H. Mousavi, A. Alù, Topologically robust sound propagation in an angular-momentum-biased graphene-like resonator lattice. *Nat. Commun.* **6**, 8260 (2015).
4. A. Souslov, K. Dasbiswas, M. Fruchart, S. Vaikuntanathan, V. Vitelli, Topological waves in fluids with odd viscosity. *Phys. Rev. Lett.* **122**, 128001 (2019).
5. P. Delplace, J. B. Marston, A. Venaille, Topological origin of equatorial waves. *Science* **358**, 1075–1077 (2017).
6. M. A. Bandres *et al.*, Topological insulator laser: Experiments. *Science* **359**, eaar4005 (2018).
7. O. Zilberberg *et al.*, Photonic topological boundary pumping as a probe of 4D quantum hall physics. *Nature* **553**, 59–62 (2018).
8. Y. E. Kraus, Y. Lahini, Z. Ringel, M. Verbin, O. Zilberberg, Topological states and adiabatic pumping in quasicrystals. *Phys. Rev. Lett.* **109**, 106402 (2012).
9. M. Lohse, C. Schweizer, O. Zilberberg, M. Aidelsburger, I. Bloch, A Thouless quantum pump with ultracold bosonic atoms in an optical superlattice. *Nat. Phys.* **12**, 350–354 (2015).
10. R. P. Pedro, J. Paulose, A. Souslov, M. Dresselhaus, V. Vitelli, Topological protection can arise from thermal fluctuations and interactions. *Phys. Rev. Lett.* **122**, 118001 (2019).
11. J. M. Zeuner *et al.*, Observation of a topological transition in the bulk of a non-Hermitian system. *Phys. Rev. Lett.* **115**, 040402 (2015).
12. Z. Gong *et al.*, Topological phases of non-Hermitian systems. *Phys. Rev. X* **8**, 031079 (2018).
13. H. Shen, B. Zhen, L. Fu, Topological band theory for non-Hermitian Hamiltonians. *Phys. Rev. Lett.* **120**, 146402 (2018).
14. A. Ghatak, T. Das, New topological invariants in non-Hermitian systems. *J. Phys. Condens. Matter* **31**, 263001 (2019).
15. S. Yao, Z. Wang, Edge states and topological invariants of non-Hermitian systems. *Phys. Rev. Lett.* **121**, 086803 (2018).
16. F. K. Kunst, E. Edvardsson, J. C. Budich, E. J. Bergholtz, Biorthogonal bulk-boundary correspondence in non-Hermitian systems. *Phys. Rev. Lett.* **121**, 026808 (2018).
17. C. H. Lee, R. Thomale, Anatomy of skin modes and topology in non-Hermitian systems. *Phys. Rev. B* **99**, 201103 (2019).
18. T. Helbig *et al.*, Generalized bulk–boundary correspondence in non-Hermitian topolectrical circuits. *Nat. Phys.* **16**, 747–750 (2020).
19. E. J. Bergholtz, J. C. Budich, F. K. Kunst, Exceptional topology of non-Hermitian systems. arXiv:1912.10048 (20 December 2019).
20. L. Xiao *et al.*, Non-Hermitian bulk–boundary correspondence in quantum dynamics. *Nat. Phys.* **16**, 761–766 (2020).
21. V. M. Martinez Alvarez, J. E. Barrios Vargas, L. E. F. Foa Torres, Non-Hermitian robust edge states in one dimension: Anomalous localization and eigenspace condensation at exceptional points. *Phys. Rev. B* **97**, 121401(R) (2018).
22. T. Yoshida, Y. Hatsugai, Exceptional rings protected by emergent symmetry for mechanical systems. *Phys. Rev. B* **100**, 054109 (2019).
23. M. Z. Hasan, C. L. Kane, Colloquium: Topological insulators. *Rev. Mod. Phys.* **82**, 3045 (2010).
24. R. Fleury, D. L. Sounas, C. F. Sieck, M. R. Haberman, A. Alù, Sound isolation and giant linear nonreciprocity in a compact acoustic circulator. *Science* **343**, 516–519 (2014).
25. C. Coulais, D. Sounas, A. Alù, Static non-reciprocity in mechanical metamaterials. *Nature* **542**, 461–464 (2017).
26. Y. Wang *et al.*, Observation of nonreciprocal wave propagation in a dynamic phononic lattice. *Phys. Rev. Lett.* **121**, 194301 (2018).
27. C. L. Kane, T. C. Lubensky, Topological boundary modes in isostatic lattices. *Nat. Phys.* **10**, 39–45 (2014).
28. M. Brandenbourger, X. Locsin, E. Lerner, C. Coulais, Non-reciprocal robotic metamaterials. *Nat. Commun.* **10**, 4608 (2019).
29. T. C. Lubensky, C. L. Kane, X. Mao, A. Souslov, K. Sun, Phonons and elasticity in critically coordinated lattices. *Rep. Prog. Phys.* **78**, 073901 (2015).
30. S. D. Huber, Topological mechanics. *Nat. Phys.* **12**, 621–623 (2016).
31. R. Susstrunk, S. D. Huber, Classification of topological phonons in linear mechanical metamaterials. *Proc. Natl. Acad. Sci. U.S.A.* **113**, E4767–E4775 (2016).
32. J. Zak, Symmetry criterion for surface states in solids. *Phys. Rev. B* **32**, 2218 (1985).
33. A. McDonald, T. Pereg-Barnea, A. A. Clerk, Phase-dependent chiral transport and effective non-Hermitian dynamics in a bosonic Kitaev-Majorana chain. *Phys. Rev. X* **8**, 041031 (2018).
34. A. Mostafazadeh, Pseudo-Hermitian representation of quantum mechanics. *Int. J. Geom. Methods Mod. Phys.* **07**, 1191–1306 (2010).
35. D. S. Borgnia, A. J. Kruchkov, R.-J. Slager, Non-Hermitian boundary modes and topology. *Phys. Rev. Lett.* **124**, 056802 (2020).
36. H. Schomerus, Nonreciprocal response theory of non-Hermitian mechanical metamaterials: Response phase transition from the skin effect of zero modes. *Phys. Rev. Res.* **2**, 013058 (2020).